J. Plasma Phys. (2024), *vol*. 90, 905900606
Published by Cambridge University Press

doi:10.1017/S0022377824001429

Self-organization of collisionless shocks: from a laminar profile to a rippled time-dependent structure

Michael Gedalin [1],† **and Vadim Roytershteyn** [2]

[1]Department of Physics, Ben-Gurion University of the Negev, Beer-Sheva, Israel

[2]Space Science Institute, Boulder, CO 80301, USA

(Received 7 August 2024; revised 17 October 2024; accepted 17 October 2024)

A collisionless shock structure results from the nonlinear interaction between charged particles and electromagnetic fields. Yet, a collisionless shock is globally governed by the mass, momentum and energy conservation requirements. A stable shock structure must ensure that the fluxes of the conserved quantities are constant on average, and, therefore, is determined by this necessity. Here, we study an observed high upstream temperature high Mach number shock and show that the conservation laws cannot be fulfilled unless the shock is spatially inhomogeneous along the shock front and time-dependent.

Keywords: space plasma physics, astrophysical plasmas, plasma nonlinear phenomena

1. Introduction

Collisionless shocks are one of the most ubiquitous phenomena in space plasmas, and one of the most studied nonlinear plasma systems during the last seventy years. While the primary interest in collisionless shocks is related to their being among the most powerful accelerators of charged particles in remote astrophysical objects, like supernova remnants, or at the large scale of clusters of galaxies, the heliosphere is the only natural laboratory where these shocks can be studied in detail with *in situ* measurements. All mentioned shocks are non-relativistic magnetized fast shocks, in which the magnetic field plays a major role and the shock speed exceeds the fast magnetosonic speed. The shock structure, that is, the magnetic field inside the shock transition, and the corresponding particle motion and distributions, are the focus of the heliospheric shock studies. It is well known that the magnetic profile of fast shocks evolves with the increase of the Mach number. The concept of a shock has been born within magnetohydrodynamics (MHD), where it is treated as a discontinuity. In what follows we shall extensively use the normal incidence frame (NIF). The NIF is the frame in which a shock discontinuity stands and the plasma flow enters the shock along the shock normal with the velocity V_u (the upstream NIF velocity). Hereafter, subscript u means 'upstream' and subscript d means 'downstream', in the shock frame. In MHD, fast shocks are typically characterized by the angle θ_{Bn} between

† Email address for correspondence: gedalin@bgu.ac.il

the upstream magnetic field vector $\boldsymbol{B}_u$ and the normal to the shock front $\hat{\boldsymbol{n}}$. The latter will be assumed to point from the upstream to the downstream. A shock is also characterized by the parameter $\beta_u = 8\pi p_u/B_u^2$, where p_u is the upstream kinetic plasma pressure. The most important shock parameter is the Mach number. The Alfvénic Mach number is M_A and the fast Mach number M_F are defined as follows:

$$M_A = \frac{V_u}{v_A}, \quad M_F = \frac{V_u}{v_F}, \tag{1.1a,b}$$

$$v_A^2 = \frac{B_u^2}{4\pi n_u m_p}, \tag{1.2}$$

$$v_F^2 = \frac{1}{2}(v_A^2 + v_s^2 + \sqrt{(v_A^2 + v_s^2)^2 - 4v_A^2 v_s^2 \cos^2\theta_{Bn}}), \tag{1.3}$$

where n_u is the upstream proton number density, m_p is the proton mass and v_s is the sound speed. For simplicity, the plasma is considered to consist of protons and electrons, while possible admixtures of α-particles are ignored. The sound speed $v_s^2 = \gamma T_u/m_p$, where $T_u = p_u/n_u$ is the upstream temperature, and $\gamma = 5/3$ in isotropic plasmas. For fast shocks $M_A > M_F > 1$. The magnetic profile of a shock depends on all three parameters, M_A, θ_{Bn} and β_u. Magnetic profiles or quasi-perpendicular shocks, $\theta_{Bn} > 45^\circ$, are typically more regular than that of quasiparallel shocks, $\theta_{Bn} < 45^\circ$ (Bale *et al.* 2005; Burgess *et al.* 2005; Krasnoselskikh *et al.* 2013). Low β_u shocks are typically less structured than high β_u shocks (Greenstadt *et al.* 1975, 1977, 1980; Russell *et al.* 1982*b*; Farris, Russell & Thomsen 1993). However, the Mach number is usually considered the main parameter related to structural changes of the collisionless shock front. The Alfvénic Mach number has a simple physical meaning: the ratio of the kinetic energy flux along the shock normal $n_u m_p V_u^3$ to the Poynting flux $c(\boldsymbol{E}\times\boldsymbol{B})\cdot\hat{\boldsymbol{n}}/4\pi = V_u B_u^2/4\pi$ is M_A^2. The fast Mach number does not have such a simple energetic meaning, so we usually use M_A. Low M_A low β_u shocks are laminar, with nearly monotonically increasing magnetic field magnitude. The dissipative MHD relates changes in the structure to the absence of shock solutions with resistivity and thermal conduction alone above the so-called critical Mach number, at which the downstream flow velocity along the shock normal drops below the downstream sound speed (Kennel 1987, 1988). Above the critical Mach number, viscosity is necessary. This critical Mach number is often considered to mark the onset of ion reflection. However, theoretically, ion reflection and the accompanying appearance of overshoot and downstream magnetic oscillations were predicted for dispersive shocks, where above some critical Mach number a soliton solution is not possible (Sagdeev 1966). The two critical Mach numbers are different, the dissipative one being smaller than the dispersive one (Forslund & Freidberg 1971; Manheimer & Spicer 1985). Yet, traditionally deviation from the monotonic shape and onset of ion reflection was attributed to crossing the dissipative critical Mach number (Livesey, Kennel & Russell 1982; Russell, Hoppe & Livesey 1982*a*), and up to now shocks are often classified as subcritical or supercritical (Zhou & Smith 2015). It was found observationally that ion reflection and overshoot occur in subcritical shocks as well (Farris *et al.* 1993). It has been shown, observationally, theoretically and in simulations, that even in very low Mach number shocks overshoot and downstream magnetic oscillations develop due to the transmitted ion gyration and slow gyrophase mixing and kinematic collisionless relaxation (Balikhin *et al.* 2008; Ofman *et al.* 2009; Gedalin 2015; Gedalin, Friedman & Balikhin 2015). Overshoots are stronger in higher Mach number shocks (Livesey *et al.* 1982; Russell *et al.* 1982*a*; Tatrallyay, Luhmann & Research 1984; Scudder *et al.* 1986; Mellott & Livesey

https://doi.org/10.1017/S0022377824001429 Published online by Cambridge University Press

1987; Tatrallyay *et al.* 1997; Masters *et al.* 2013), which was thought, until recently, due to reflected ions. Low Mach number shocks are planar and time stationary, to a very good approximation. Even at rather high Mach numbers, a shock may be planar and time stationary (Scudder *et al.* 1986). It was shown that, in moderately supercritical shocks, the magnetic profile is consistent with the kinematic collisionless relaxation and may be only weakly non-planar or time-dependent (Gedalin 2019*a*,*b*,*c*). At sufficiently high Mach numbers, shocks become rippled (Moullard *et al.* 2006; Lobzin *et al.* 2008; Ofman & Gedalin 2013; Johlander *et al.* 2016; Gingell *et al.* 2017; Johlander *et al.* 2018) or reforming (Lobzin *et al.* 2007; Lefebvre *et al.* 2009; Tiu *et al.* 2011; Sundberg *et al.* 2013; Dimmock *et al.* 2019; Liu *et al.* 2021). It was suggested that onset of time dependence occurs when the so-called whistler critical Mach number is exceeded (see, e.g. Krasnoselskikh *et al.* 2013), and the upstream whistler waves can no longer stand in the shock frame.

All the above approaches, striving to explain the observed structural changes in the magnetic profile with the increase of the Mach number, focus on nonlinear wave features or details of the ion dynamics. Indeed, ions carry most of mass, momentum and energy, and therefore ions shape the profile. However, we suggest that the kind of shock structure (laminar, planar and stationary structured, rippled, reforming or whatever else will be observed in the future) is independent of the exact mechanism causing the structure, and is determined by the necessity to ensure stable transfer of mass, momentum and energy across the shock. By stable we mean that on average the fluxes of the above-mentioned conserved quantities should be constant and there should be no large disruptions in the transfer. We suggest that a collisionless shock is a self-regulatory system, and the shock structure is the one that ensures the stability of the mass, momentum and energy fluxes, for given upstream parameters. Within this approach, the focus is shifted from reason to purpose: more than one microscopic process may lead to the same type of collisionless shock structure, which is determined solely by the requirement of stable fluxes. In other words, this means that if the conservation laws can be fulfilled with a laminar profile, the shock will be laminar. With the increase of the Mach number, this is no longer possible, and the shock develops a structure, no matter what it is the mechanism of the structure generation. It has been shown that, in higher Mach number shocks, necessary ion heating requires stronger ion reflection, which in turn requires the development of an overshoot (Gedalin *et al.* 2023*a*). The mechanism of the overshoot formation is due to the deceleration of the transmitted ion flow, while the reflected ions limit overshoot growth, thus ensuring stability (Gedalin & Sharma 2023; Sharma & Gedalin 2023). Here, we show that, at even higher Mach numbers, a planar stationary structure cannot ensure stable mass, momentum and energy conservation, which means that the shock front becomes rippled.

2. Observations

In this section, we describe observations of a shock which is modelled in the rest of the paper. Figure 1 shows the magnitude and three components of the magnetic field, measured by MMS1 on 22 April 2020 at 16:43:50 UTC. The resolution corresponds to the FGM survey mode (Russell *et al.* 2016; Torbert *et al.* 2016). The fields are rotated into the shock coordinates, as follows: the x-coordinate is along the model shock normal (Farris & Russell 1994), $\hat{\boldsymbol{n}} = (0.6720, -0.7152, 0.1921)$ in the GSE coordinates, pointing toward downstream, the z-coordinate is along the difference between the downstream and upstream magnetic field vectors $\Delta\boldsymbol{B} = \boldsymbol{B}_d - \boldsymbol{B}_u$ and the non-coplanarity direction is $\hat{\boldsymbol{y}} = \hat{\boldsymbol{z}} \times \hat{\boldsymbol{x}}$. The upstream region is chosen visually as $-166 < t < -86$ (in seconds from the crossing), and the downstream region is $212 < t < 447$. The angle between the upstream magnetic field and the shock normal $\theta_{Bn} = 115^\circ$. The magnetic compression $B_d/B_u = 2.9$. The upstream and downstream ions and electron number densities $n_{iu} = 3.0\,\mathrm{cm}^{-3}$,

https://doi.org/10.1017/S0022377824001429 Published online by Cambridge University Press

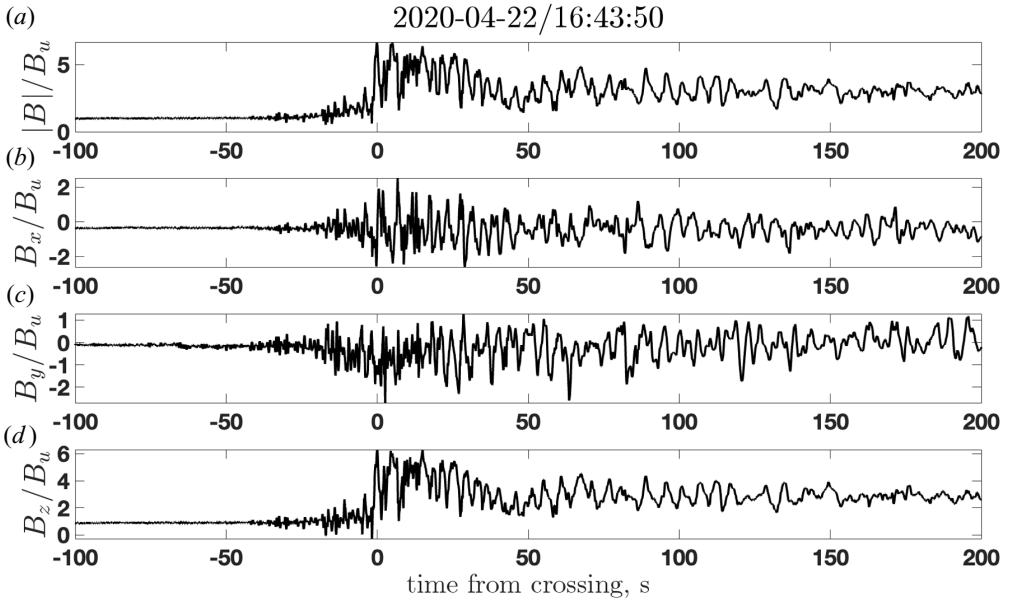

FIGURE 1. The magnitude and three components of the magnetic field, measured by MMS1 on 22 April 2020 at 16:43:50 UTC. The components are given in the shock frame, see details in the text.

$n_{eu} = 2.3\,\mathrm{cm}^{-3}$, $n_{id} = 9.7\,\mathrm{cm}^{-3}$ and $n_{ed} = 9.8\,\mathrm{cm}^{-3}$ are taken from plasma measurements by FPI (Pollock *et al.* 2016). The upstream densities differ, although quasi-neutrality is supposed to hold. The Alfvén speed, the shock speed and the upstream plasma velocity in NIF are calculated as

$$V_A = 21.8\frac{B_u}{\sqrt{n_u}}\,\mathrm{km\,s}^{-1}, \tag{2.1}$$

$$V_{sh} = \frac{(n_d\boldsymbol{V}_2 - n_u\boldsymbol{V}_1)\cdot\hat{\boldsymbol{n}}}{n_d - n_u}, \tag{2.2}$$

$$V_u = \frac{n_d}{n_d - n_u}|(\boldsymbol{V}_1 - \boldsymbol{V}_2)\cdot\hat{\boldsymbol{n}}|, \tag{2.3}$$

where $\boldsymbol{V}_1$ and $\boldsymbol{V}_2$ are the plasma velocities in the upstream and downstream regions, as measured by the spacecraft. When using the electron velocities $\boldsymbol{V}_{e1}\cdot\hat{\boldsymbol{n}} = 301.5\,\mathrm{km\,s}^{-1}$, $\boldsymbol{V}_{e2}\cdot\hat{\boldsymbol{n}} = 76.0\,\mathrm{km\,s}^{-1}$ and densities in (2.1)–(2.3), the shock speed has a wrong sign, so we use the ion velocities $\boldsymbol{V}_{i1}\cdot\hat{\boldsymbol{n}} = 291.0\,\mathrm{km\,s}^{-1}$, $\boldsymbol{V}_{i2}\cdot\hat{\boldsymbol{n}} = 76.5\,\mathrm{km\,s}^{-1}$, which give $v_A \approx 38\,\mathrm{km\,s}^{-1}$, $V_u \approx 308\,\mathrm{km\,s}^{-1}$ and $M_A = V_u/v_A \approx 8$. The upstream $\beta_{iu} = 7.8$ and $\beta_{eu} = 6.1$, as calculated onboard. For $\beta_u \approx 10$ the fast Mach number $M_F \approx 2.5$. In what follows we use the upstream ion gyrofrequency $\Omega_u = eB_u/m_pc$ and the ion inertial length c/ω_{pi}, $\omega_{pi}^2 = 4\pi n_u e^2/m_p$.

The non-coplanar component of the magnetic field B_y makes excursion toward negative values inside the central part of the transition, in qualitative agreement with the theoretically derived relation $B_y \propto \cos\theta_{Bn}(\mathrm{d}B_z/\mathrm{d}z)$ (see, e.g. Gedalin *et al.* 2022). On the other hand, the strong fluctuations of B_x inside the central part clearly indicate the non-planarity of the shock front (Gedalin & Ganushkina 2022). The maximum magnetic field is $B_m/B_u \approx 6.7$. The tangential components of the upstream plasma velocity in the

https://doi.org/10.1017/S0022377824001429 Published online by Cambridge University Press

spacecraft frame are $V_y \approx 130\,\mathrm{km\,s^{-1}}$ and $V_z \approx -260\,\mathrm{km\,s^{-1}}$. The shock speed in the spacecraft frame is $V_{sh} \approx -17\,\mathrm{km\,s^{-1}}$. This means that the spacecraft crosses the shock tangentially, at an angle $\approx 87^\circ$ to the shock normal, and at an angle $\approx 27^\circ$ to z-direction.

3. Modelling

The principles of the approach are as follows: we numerically trace ions across a model shock front, derive the total pressure $p_{xx} = m_p\langle \int v_x^2 f(\boldsymbol{r}, \boldsymbol{v}, t)\,\mathrm{d}^3\boldsymbol{v}\rangle$ of the generated ion distribution and analyse whether this pressure is consistent with the model shock profile used for the tracing. Here, $f(\boldsymbol{r}, \boldsymbol{v}, t)$ is the ion distribution function, and $\langle(\cdots)\rangle$ denotes proper spatial and temporal averaging, if such is needed. In this approach, mass conservation is fulfilled automatically. We restrict ourselves to one component of the pressure only. A more sophisticated approach, taking into account also p_{yx}, p_{zx} and the energy flux, would be beyond any possible precision of the model. Initially, ions are distributed according to the Maxwellian distribution with the thermal speed $v_T = V_u\sqrt{\beta_{iu}/2}/M_A$. The method was described in detail by Gedalin (2016). The electron pressure is taken into account in the adiabatic approximation $p_e/n^{5/3} = \mathrm{const}$. Note that we are not going to reproduce the profile or any of the details of the shock described in § 2. Given the uncertainties of measurements and errors in the determination of the shock parameters, this task would be impossible. The objective of the present study is to analyse whether a shock with the parameters in the observed range, that is, a quasi-perpendicular high Mach number, high-β shock can be laminar or structured planar stationary, or the stability of the fluxes of the conserved quantities dictate non-planarity and dependence on time (rippling).

3.1. *Non-structured profile*

We start with the attempt to model the observed shock with a laminar profile with the calculated magnetic compression of $B_d/B_u = 2.9$. Figure 2 presents the magnetic compression B_d/B_u as a function of the Alfvénic Mach number M_A, obtained by solving the Rankine–Hugoniot relations (Kennel *et al.* 1985) for various upstream β_u. For a given B_d/B_u, higher β_u requires higher M_A. It is seen that the measured B_d/B_u and β_u are inconsistent with the derived Mach number. Since the Rankine–Hugoniot relations are nothing but conservation laws and must be fulfilled, we will choose $B_d/B_u = 2.8$, $\beta_u = 12$ and $M_A = 10$ for the modelling.

We start with a monotonic magnetic field given by the expressions

$$B_z = B_u \sin\theta_{Bn}\left(\frac{R+1}{2} + \frac{R-1}{2}\tanh\frac{3x}{D}\right) \tag{3.1}$$

$$B_x = B_u \cos\theta_{Bn} \tag{3.2}$$

$$B_y = \frac{c\cos\theta_{Bn}}{M_A\omega_{pi}}\frac{\mathrm{d}B_z}{\mathrm{d}x} \tag{3.3}$$

$$\frac{B_d}{B_u} = \sqrt{R^2\sin^2\theta_{Bn} + \cos^2\theta_{Bn}}. \tag{3.4}$$

The expression (3.3) has been derived within a two-fluid study of stationary nonlinear waves (Gedalin 1998). These expressions should be completed with the electric field, which takes the form: $E_z = 0$, $E_y = V_u B_u \sin\theta_{Bn}/c$ and $E_x = -K_E B_y$. The coefficient K_E is

https://doi.org/10.1017/S0022377824001429 Published online by Cambridge University Press

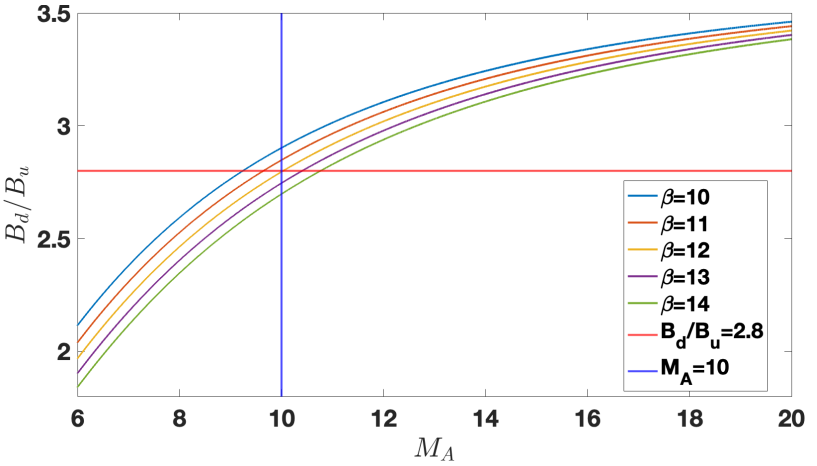

FIGURE 2. The magnetic compression B_d/B_u as a function of the Alfvénic Mach number M_A, for various β_u, as obtained from the solution of the Rankine–Hugoniot relations (Kennel, Edmiston & Hada 1985).

determined by the value of the cross-shock potential

$$e\phi = -\int E_x \,\mathrm{d}x = s(m_p V_u^2/2), \tag{3.5}$$

where s is one of the varied parameters of modelling. The ramp width is chosen as $D = c/\omega_{pi}$.

Figure 3 presents the reduced distribution function $f(x, v_x) = \int f(x, \boldsymbol{v})\,\mathrm{d}v_y\,\mathrm{d}v_z$. Heating occurs mainly due to the downstream gyration of the directly transmitted ions. Reflected ions contribute a small part. The kinematic collisionless relaxation due to the gyrophase mixing is seen very clearly. The decisive step is the calculation of the magnetic field from the conservation law

$$p_{xx} + \left(\frac{n}{n_u}\right)^{5/3}(n_u T_u) + \frac{B^2}{8\pi} = n_u m_p V_u^2 + 2n_u T_u + \frac{B_u^2}{8\pi}, \tag{3.6}$$

where $n = \int f(x, v_x)\,\mathrm{d}v_x$. This magnetic field is shown in figure 4. It is seen that the calculated magnetic field approaches the model magnetic field well behind the shock transition. It should be mentioned that the result is sensitive to the value of s. At first sight, the model is successful. However, in a planar stationary shock the equation (3.6) should be valid throughout the shock, for each position x. However, figure 4 shows that (3.6) requires that the shock profile be structured. In particular, the shock structure should include a large overshoot. We, therefore, move on to modelling a structured planar stationary shock. Such shocks were shown to exist (Scudder *et al.* 1986).

3.2. *A structured planar stationary shock model*

Our objective is to model a structured shock profile, which would include at least a foot and an overshoot and would be similar to the observed shock profile, but not necessarily reproduce the latter. Such modelling requires first denoising the magnetic profile, that is, removing oscillations that are supposed not to be a part of the shock structure but, possibly, transient waves or observed due to the tangential crossing of the shock by the spacecraft.

https://doi.org/10.1017/S0022377824001429 Published online by Cambridge University Press

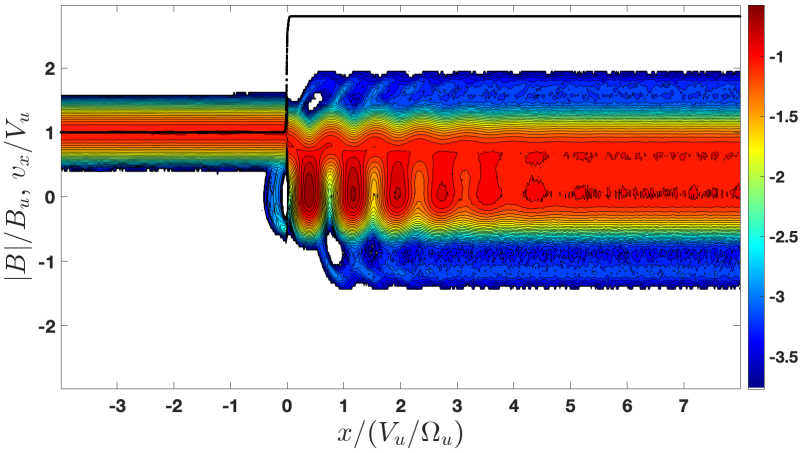

FIGURE 3. The reduced distribution function $f(x, v_x) = \int f(x, \boldsymbol{v})\, \mathrm{d}v_y\, \mathrm{d}v_z$ obtained by tracing 80 000 ions through the shock profile given by (3.1)–(3.3) and $s = 0.32$.

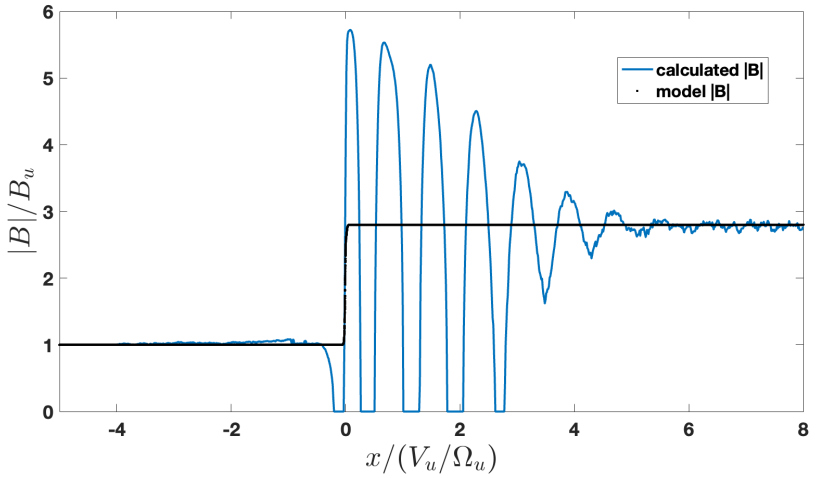

FIGURE 4. The magnetic field calculated from (3.6).

Figure 4 makes the impression that at least one magnetic maximum corresponds to the overshoot, after which the magnetic field drops to the downstream value or below it. The position of the overshoot corresponds to the position of the maximal deceleration of the directly transmitted ions in figure 3. Figure 3 also shows that the reflected ions appear as far as approximately $0.5(V_u/\Omega_u)$ from the ramp. This distance should approximately correspond to the foot length of a structured shock. Figure 5 compares the original profile with a denoised one. The latter is obtained by applying Daubechies 10 wavelet transform, reducing the smaller scale 9 levels, and applying the inverse transform (WaveShrink procedure of the WaveLab 850 package).

An overshoot is added as follows:

$$\Delta B_z = aB_u \sin\theta_{Bn} g(x, x_l, w_l, x_r, w_r) \tag{3.7}$$

$$g(x, x_l, w_l, x_r, w_r) = \left(1 + \tanh\frac{3(x - x_l)}{w_l}\right)\left(1 - \tanh\frac{3(x - x_r)}{w_r}\right). \tag{3.8}$$

https://doi.org/10.1017/S0022377824001429 Published online by Cambridge University Press

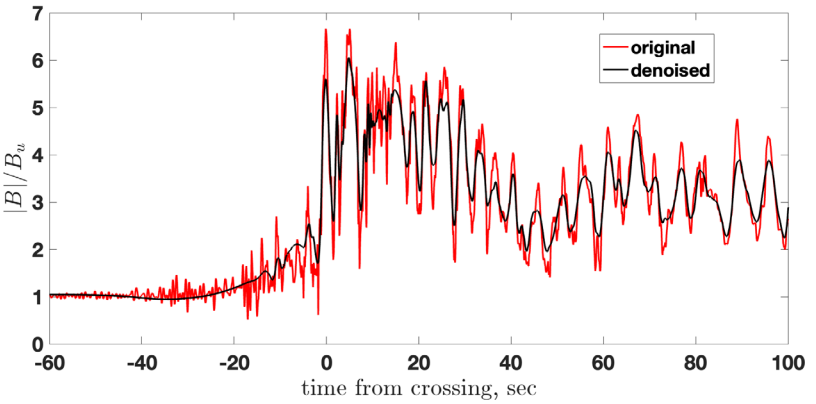

FIGURE 5. The original magnetic field magnitude truncated to 2^{13} points (red) and the denoised magnetic field. The denoising is done by applying Daubechies 10 wavelet transform, reducing the smaller scale 9 levels, and applying the inverse transform.

For the run below the following parameters are chosen: $a = 1$, $w_l = 0.3(V_u/\Omega_u)$, $w_r = 1.87(V_u/\Omega_u)$, $x_l = 0.1(V_u/\Omega_u)$, $x_r = 0.15(V_u/\Omega_u)$. Because of the overshoot, the cross-shock potential has to be modified, so the downstream value $s_d = 0.2$ while $s_{\max} = 0.35$.

Figure 6 shows the reduced distribution function $f(x, v_x)$, in the format similar to figure 3. It has been shown that an overshoot enhances ion reflection (Gedalin *et al.* 2023*a*). This enhancement is easily seen comparing figures 3 and 6. Ion reflection is strong because of the large $v_T/v_u = 0.17$ (Sharma & Gedalin 2023). The much larger fraction of the reflected ions in the structured shock reverses the behaviour of the total ion pressure p_{xx} across the shock from decreasing, as required by the conservation laws, to increasing, which is impossible in a stable shock. Although figure 7 shows this behaviour for one set of parameters but it has been found that no variation of parameters can reduce the far downstream p_{xx} to below the upstream value. Thus, the observed profile (figures 1 and 5) cannot belong to a planar stationary shock. Namely, rippling should be explored as the next viable possibility.

3.3. *A rippled shock: simulations*

A self-consistent two-dimensional (2-D) hybrid kinetic simulation was performed in order to provide a reference configuration for the modelling effort. In the hybrid simulation model, the ions are treated kinetically, while electrons are modelled as a massless fluid with a prescribed equation of state (e.g. Winske *et al.* 2023). The simulation was performed in a 2-D domain of size $L_x \times L_y = (1024 \times 256)(c/\omega_{pi})$, covered by a uniform grid with 8192×2048 cells. The upstream parameters are $\theta_{Bn} = 115^\circ$ and $\beta_e = \beta_i = 6$, where the distribution function for the ions is a drifting Maxwellian. The upstream magnetic field is in the x–y plane. Note that the y-coordinate in the simulation corresponds to the z-coordinate in the data and test particle analyses. The plasma is injected from $x = 0$ of a 2-D simulation domain with the speed $V_0 = 7V_A$. Reflecting boundary conditions are used at $x = L_x$, and the shock is formed by the interaction between the incoming and reflecting flows. In the simulation frame of reference, the shock propagates in the negative x direction with the average speed $V_{sh} \approx 3.35V_A$, resulting in total upstream flow in the NIF $V_u \approx 10.35V_A$. The simulation was performed using a version of the H3D code (Karimabadi *et al.* 2006) adapted for shock simulations. An adiabatic equation of state

https://doi.org/10.1017/S0022377824001429 Published online by Cambridge University Press

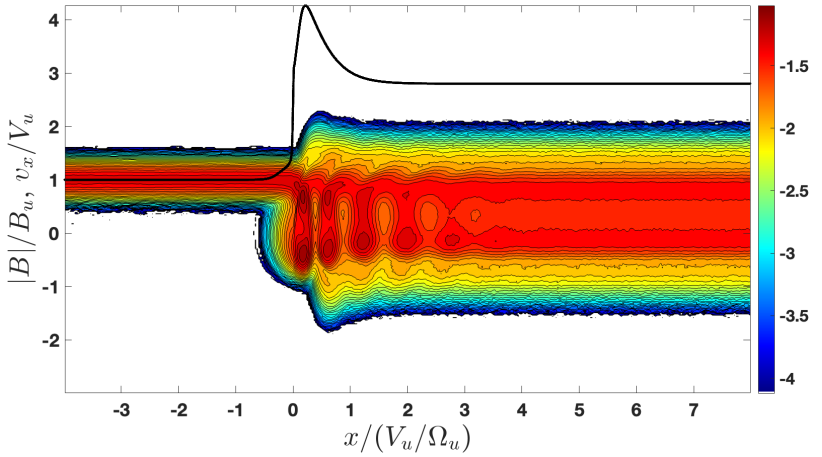

FIGURE 6. The reduced distribution function $f(x, v_x) = \int f(x, \boldsymbol{v})\, \mathrm{d}v_y\, \mathrm{d}v_z$ obtained by tracing 80 000 ions through the structured shock profile. The black line shows the magnetic field magnitude.

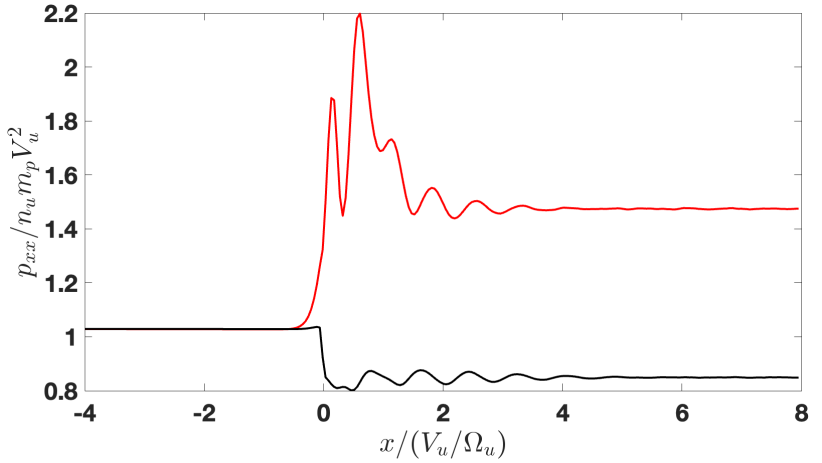

FIGURE 7. Ion p_{xx} throughout the shock. Black line: the non-structured shock. Red line: the planar stationary structured shock.

with adiabatic index $\gamma = 5/3$ was used for the electrons. Ion distribution is sampled by computational particles with a uniform and constant statistical weight, such that in the upstream region the number of particles per cell is $N_{\mathrm{ppc}} = 100$. The time step used in the simulation is $\delta t\Omega_u = 1.25 \times 10^{-3}$. In the discussion below, coordinates are normalized to upstream ion inertial length c/ω_{pi}, while time is normalized to Ω_u.

The basic properties of the shock are summarized in figure 8, which shows x-profiles of the magnetic field components $B_x(x', y = \mathrm{const}, t\Omega_u = 125)/B_u$, $B_y(x', y = \mathrm{const}, t\Omega_u = 125)/B_u$, normal component of the velocity $V_x'(x', y = \mathrm{const}, t\Omega_u = 125)/V_u$ and density $\rho(x', y = \mathrm{const}, t\Omega_u = 125)/\rho_u$, taken at various values of $y = \mathrm{const}$ (left column). Here, $V_x' = V_x + V_{sh}$ is the velocity in NIF. There is substantial variance of the above variables.

https://doi.org/10.1017/S0022377824001429 Published online by Cambridge University Press

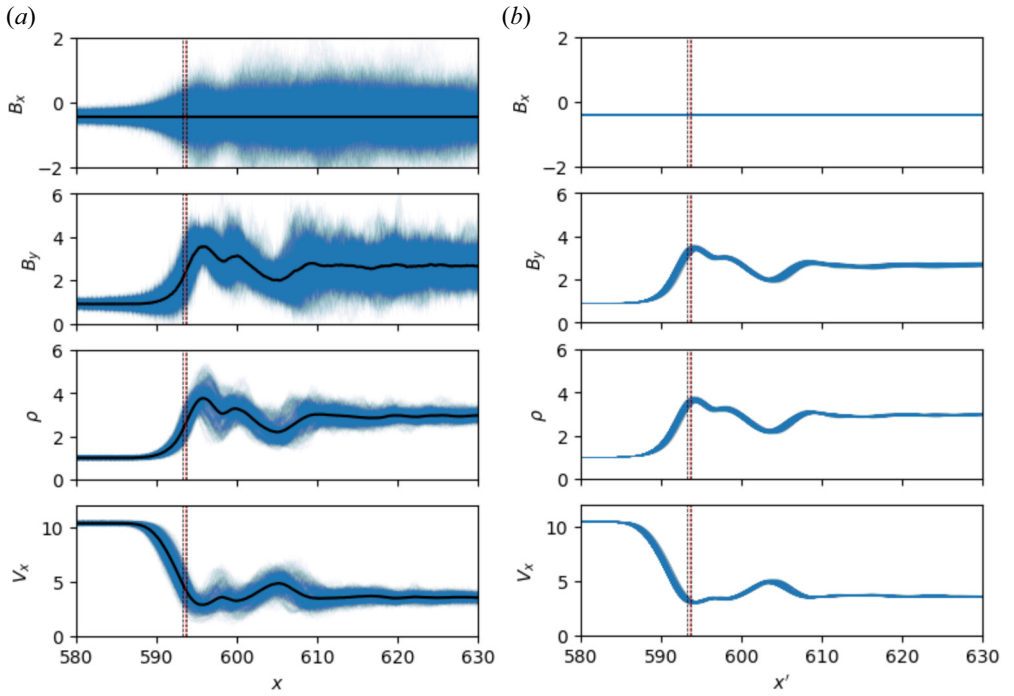

FIGURE 8. Profiles of (top to bottom) B_x, B_y, ρ and V_x in the hybrid simulation. The left column shows $y = \text{const}$ cuts taken at each cell, i.e. there are 2048 cuts, and a single instance of time $t\Omega_u = 125$. In each panel, each blue line is the single profile, e.g. $B_y(x, y = const, t = \text{const})$, while the black line corresponds to the y-average. The vertical dash lines mark the region used in the analysis of shock front perturbations and distribution function below. The right column shows $\langle B_x\rangle_y(x', t)$, $\langle B_y\rangle_y(x', t)$, $\langle V'_x\rangle_y(x', t)$ and $\langle\rho\rangle_y(x', t)$, for various moments in the time interval $125 < t\Omega_u < 220$. Here, $x' = x + V_u(t - t_0)$ is the NIF coordinate, with $t_0\Omega_u = 125$, and $V_x = V'_x + V_{sh}$.

The right column shows the y-averaged profiles

$$\langle X\rangle_y(x', t) = \frac{1}{L_y}\int \mathrm{d}y X(x', y, t), \tag{3.9}$$

where $X = B_x, B_y, V_x, \rho$, for various moments in the time interval $125 < t\Omega_u < 220$, and $x' = x + V_u(t - t_0)$ is the NIF coordinate. The y-average profiles are stationary in NIF.

The structure of the shock front perturbations is further illustrated in figure 9, which shows a section of the simulation domain of size $(60 \times 60)c/\omega_{pi}$ near the shock front. Several distinct types of perturbations are present, with different wavelengths and polarization properties. We identify the shock rippling by the enhancements at the shock front, shown in the figure by red arrows. The wavelength of these fluctuations is approximately $25c/\omega_{pi}$. These perturbations propagate in the negative y-direction, with the velocity $V_y \approx -6V_A$. Note that the fronts of the rippling wave are not perpendicular to the shock front but are oblique. One of these fronts is along a red arrow in the figure. Figure 10 illustrates the frequency spectrum of B_y fluctuations along the shock front in the NIF. The spectrum is obtained by performing the fast Fourier transform of B_y collected in a narrow region around $x' = 593.5c/\omega_{pi}$ (see figure 8). The spectrum shows the existence of perturbations with wavenumbers in the range $k_y \lesssim 0.6$, propagating roughly with the

https://doi.org/10.1017/S0022377824001429 Published online by Cambridge University Press

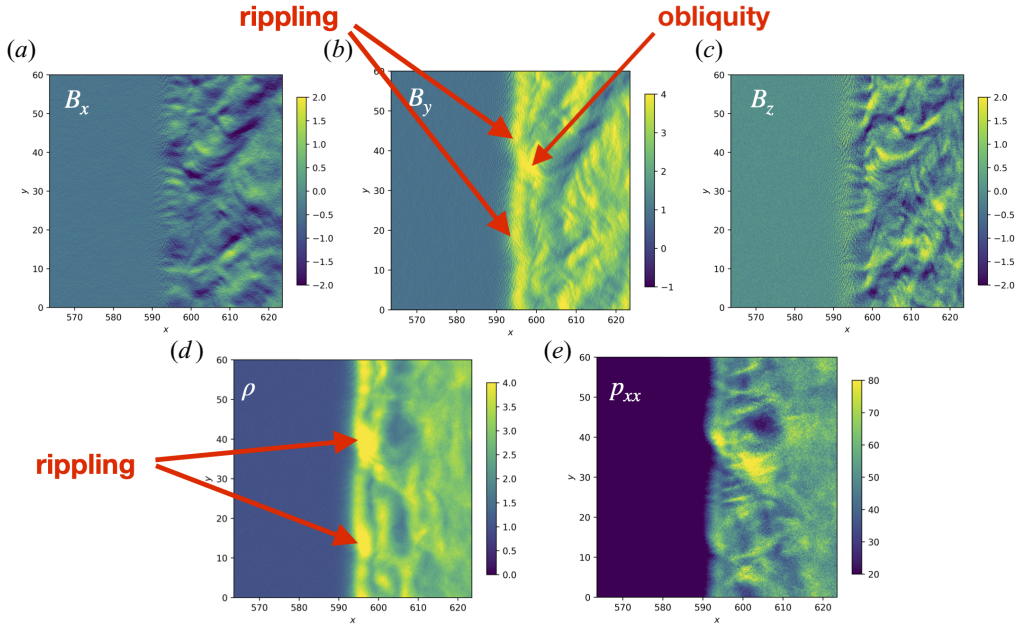

FIGURE 9. Two-dimensional profiles of (clockwise) B_x, B_y, B_z, ρ and pressure tensor $\hat{p}_{xx}$ in a hybrid simulation at $t\Omega_u = 125$.

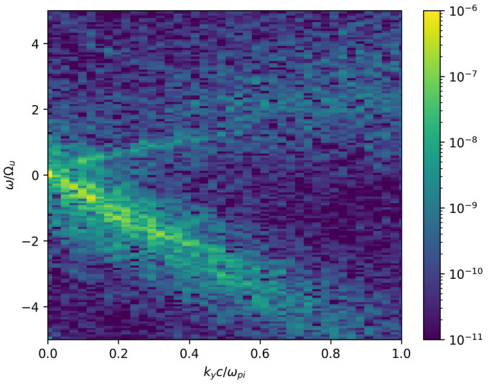

FIGURE 10. Frequency–wavenumber spectrum of B_y fluctuations along the shock front.

same phase speed in the negative y direction. Further, there appears to exist a second class of weaker fluctuations, propagating in the opposite direction with a somewhat smaller phase speed.

The reduced ion distribution function collected in the same narrow region of x is shown in figure 11. The same rippling as in figure 9 is seen in the reduced distribution function and is marked by red arrows. The rippling seems to be closely related to the non-locality of the reflection process is also seen (Gedalin 2023).

Despite the spatial and time variability of the shock structure, the shock maintains stable average fluxes of the conserved quantities, as expected. This is shown in figure 12, which shows fluxes of mass F_m, total momentum F_p and total energy F_ϵ in the simulation, normalized to their corresponding upstream values. Omitting resistivity terms, the

https://doi.org/10.1017/S0022377824001429 Published online by Cambridge University Press

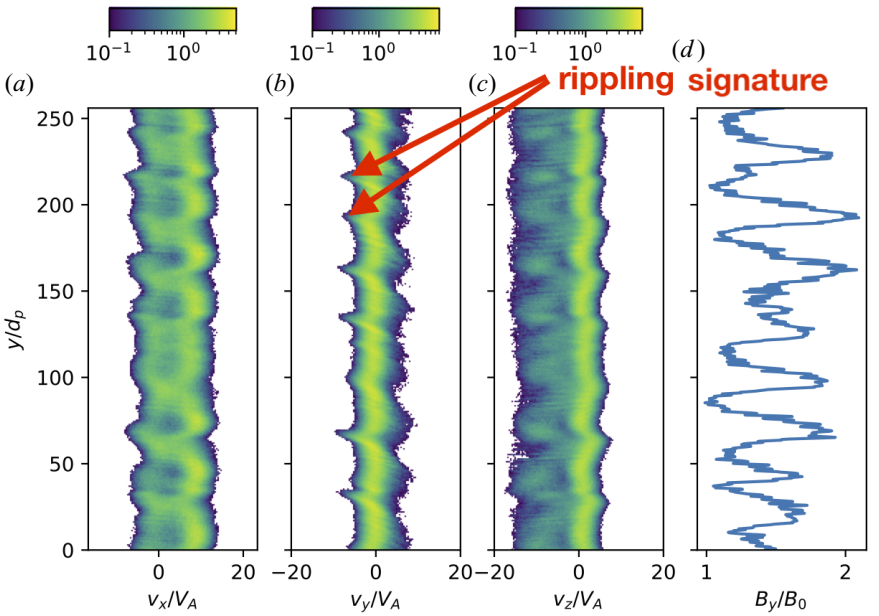

FIGURE 11. Reduced distribution function at the shock front (left to right): $f(y, v_x)$, $f(y, v_y)$, $f(y, v_z)$. The rightmost panel shows $B_y(y)$ at the same x-location. The distributions are shown in the NIF.

conserved fluxes take the following form in the hybrid model:

$$F_m = n_i V_i, \tag{3.10}$$

$$F_p = \hat{p}_{i,xx} + m_i n_i V_{ix}^2 + p_e + \frac{1}{4\pi}\left(\frac{B^2}{2} - B_x^2\right), \tag{3.11}$$

$$F_\epsilon = \chi_{i,x} + (\boldsymbol{V}_i \cdot \hat{p}_i)_x + \frac{1}{2} m_i n_i V_i^2 V_{ix} + \frac{1}{2}\mathrm{Tr}(\hat{p}_i) V_{ix} + \frac{\gamma}{\gamma - 1} p_e V_{ex} + \frac{c}{4\pi}(\boldsymbol{E} \times \boldsymbol{B})_x, \tag{3.12}$$

where

$$\hat{p}_{i,ab}(x', y, t) = m_p \int (v_a - V_a)(v_b - V_b) f(\boldsymbol{v}, x', y, t)\, \mathrm{d}^3\boldsymbol{v}, \tag{3.13}$$

is the ion kinetic pressure tensor in the co-moving frame, and

$$\chi_{i,x} = \frac{1}{2} m_p \int (\boldsymbol{v} - \boldsymbol{V})^2 (v_x - V_x) f(\boldsymbol{v}, x', y, t)\, \mathrm{d}^3\boldsymbol{v}, \tag{3.14}$$

is the ion heat flux. The fluxes in (3.10)–(3.12) are further y-averaged. We observe that time-averaged fluxes of mass and momentum are conserved to approximately 0.5 % or better between the upstream and downstream regions. The average energy flux shows somewhat greater variation, a little over 1 %, across the region included in figure 12. This is likely due to a combination of numerical dissipation in the simulation and slight time variability of the upstream conditions (which could be traced to numerical dissipation in the upstream region).

https://doi.org/10.1017/S0022377824001429 Published online by Cambridge University Press

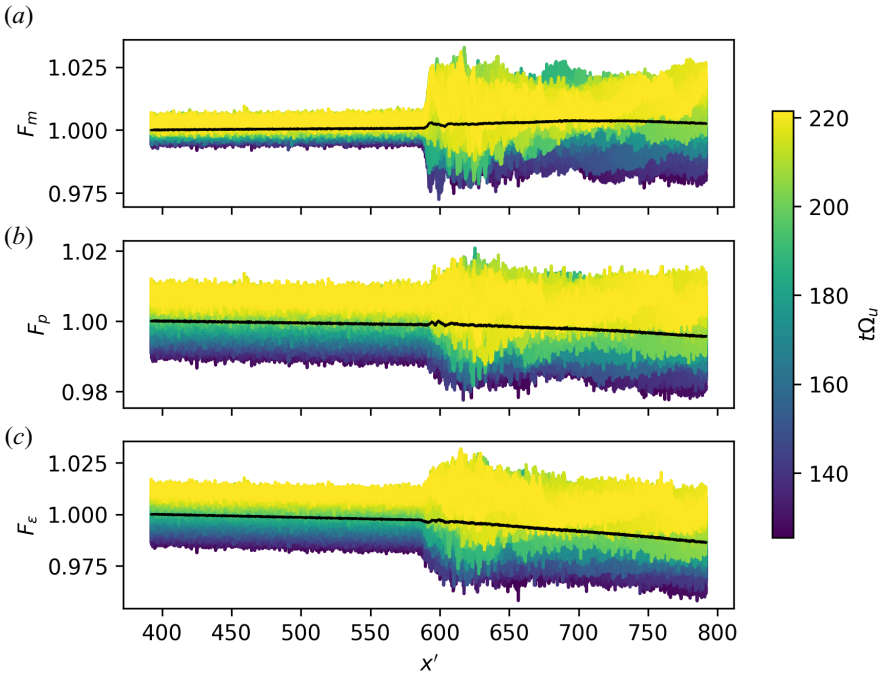

FIGURE 12. Fluxes of (top to bottom) mass, momentum and energy in the hybrid simulation. In each panel, the coloured lines show flux computed at an instance of time as indicated by the colour bar. The black lines show time-averaged fluxes. Each flux is normalized by its upstream value.

3.4. *A rippled shock: modelling*

We model a rippled shock front assuming that the shock is approximately stationary in the frame moving with the ripples along the shock front with the ripple velocity $V_u(V_{ry}, V_{rz})$. We assume that the residual time dependence seen in the simulations is of secondary importance and may be ignored when modelling the shock structure. In what follows we exploit the principles proposed by Gedalin & Ganushkina (2022). In the rippling frame, the upstream plasma velocity is $V_u(1, -V_{ry}, -V_{rz})$, so that the electric field would be

$$E_x^{(0)} = -V_{ry}\sin\theta_{Bn} - K_E\frac{\mathrm{d}B_z}{\mathrm{d}x} \tag{3.15}$$

$$E_y^{(0)} = \sin\theta_{Bn} + V_{rz}\cos\theta_{Bn} \tag{3.16}$$

$$E_z^{(0)} = -V_{ry}\cos\theta_{Bn}, \tag{3.17}$$

if the shock were planar, which is denoted by the superscript (0). We introduce the scalar and vector potentials

$$A_y^{(0)}, \quad \frac{\partial A_y^{(0)}}{\partial x} = B_z^{(0)}(x), \tag{3.18a,b}$$

$$A_z^{(0)}, \quad \frac{\partial A_z^{(0)}}{\partial y} = B_x^{(0)}, \quad -\frac{\partial A_z^{(0)}}{\partial x} = B_y^{(0)}, \tag{3.19a–c}$$

$$\phi = V_{ry}\sin\theta_{Bn}x + K_E B_z^{(0)} - (\sin\theta_{Bn} + V_{rz}\cos\theta_{Bn})y + V_{ry}\cos\theta_{Bn}z, \tag{3.20}$$

https://doi.org/10.1017/S0022377824001429 Published online by Cambridge University Press

where $\boldsymbol{B}^{(0)}$ is given by (3.1)–(3.3). Rippling is added by replacing the dependence on x with the dependence on

$$X = x - \psi \tag{3.21}$$

$$\psi = a_r \cos(k_x x + k_y y + k_z z) G \tag{3.22}$$

$$G = g(x, x_L, w_L, x_R, w_R). \tag{3.23}$$

The shape (3.22) is a generalization of waveform proposed by Gedalin & Ganushkina (2022) and is inspired by the above simulation showing that the front of the wave is not perpendicular to the shock front. Thus, rippling is a nonlinear wave propagating at an angle to the shock front. This wave damps into the downstream region and seems to not propagate into the upstream region. This behaviour is modelled using the localization function g. The replacement $x \to X$ is to be done in the vector potential and scalar potential. Then

$$B_x = \frac{\partial A_z}{\partial y} - \frac{\partial A_y}{\partial z} = \cos\theta - \psi_y B_y^{(0)} + \psi_z B_z^{(0)} \tag{3.24}$$

$$B_y = \frac{\partial A_x}{\partial z} - \frac{\partial A_z}{\partial x} = B_y^{(0)}(1 - \psi_x) \tag{3.25}$$

$$B_z = \frac{\partial A_y}{\partial x} - \frac{\partial A_x}{\partial y} = B_z^{(0)}(1 - \psi_x) \tag{3.26}$$

$$E_x = -\frac{\partial \phi}{\partial x} = (-V_{ry}\cos\theta_{Bn} - K_E B_y^{(0)})(1 - \psi_x) \tag{3.27}$$

$$E_y = -\frac{\partial \phi}{\partial y} = \sin\theta_{Bn} + V_{rz}\cos\theta_{Bn} + V_{yr}\cos\theta_{Bn}\psi_y + K_E B_y^{(0)}\psi_y \tag{3.28}$$

$$E_z = -\frac{\partial \phi}{\partial z} = -V_{ry}\cos\theta_{Bn} + K_E B_y^{(0)}\psi_z, \tag{3.29}$$

where $B_z^{(0)} = B_z^{(0)}(X)$, $B_y^{(0)} = B_y^{(0)}(X)$ and $\psi_\xi = \partial\psi/\partial\xi$. For the present analysis, we add rippling to the non-structured shock profile (3.1). The parameters chosen to make the model resemble the simulated shock are

$$k_y = 0, \quad k_z = 2\pi/3, \quad k_x = k_z\cos(145^\circ), \quad V_{ry} = 0, \quad V_{rz} = -0.6 \tag{3.30a–e}$$

$$x_L = x_R = 0, \quad w_L = 1/M_A, \quad w_R = 8, \quad a_r = 0.75/M_A. \tag{3.31a–d}$$

The three components of the magnetic of the rippled shock model are shown in figure 13 (central part only). Figure 14 further illustrates the structure of the magnetic field of the model, showing two families of the magnetic field magnitude cuts. The model was used to trace 160 000 ions. The incident distribution was the same Maxwellian as above. The initial x and y were the same for all ions, while the initial z were randomly distributed along the wavelength $0 \le z < 3$. Figure 15 presents the results of the tracing as a 2-D distribution of the ion pressure $p_{i,xx}$, where

$$p_{i,xx}(x, z) = m_p \int v_x^2 f(\boldsymbol{v}, x, z)\, \mathrm{d}^3\boldsymbol{v}. \tag{3.32}$$

The distribution function $f(\boldsymbol{v}, x, z)$ is obtained by counting particles appearing in 500×50 cells of the size $\Delta x = 0.018$ and $\Delta y = 0.06$. During the tracing z-coordinate of an ion may

https://doi.org/10.1017/S0022377824001429 Published online by Cambridge University Press

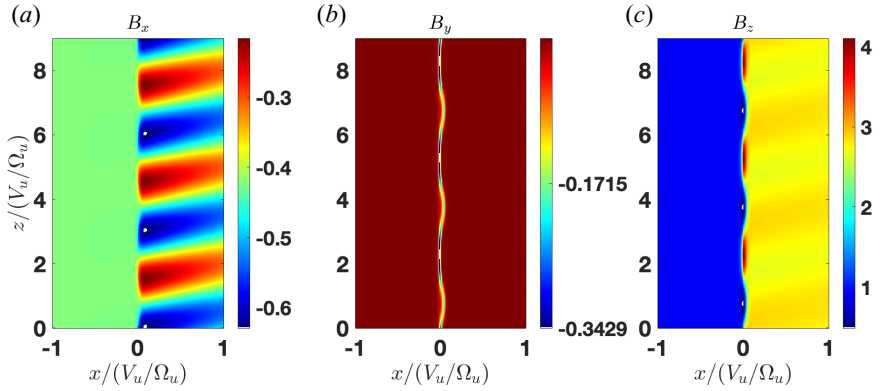

FIGURE 13. The three components of the magnetic of the rippled shock model. Three wavelengths along the shock front are shown.

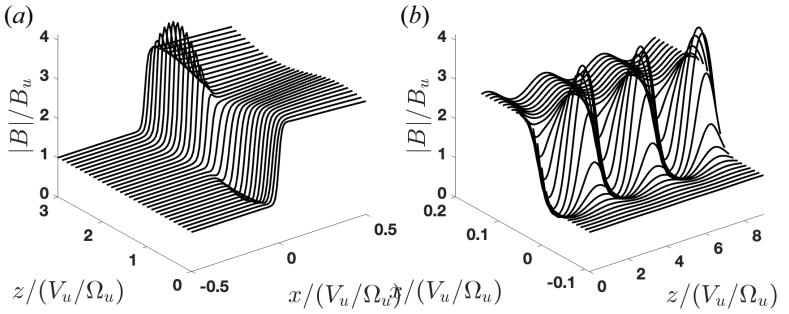

FIGURE 14. (*a*) Value of $|B|/B_u$ as a function of x for various z. (*b*) Value of $|B|/B_u$ as a function of z for various x.

leave the stripe $0 \le z < 3$. In this case, it is counted with z-coordinate shifted toward the stripe by adding an integer number of wavelengths. Each ion count is multiplied with the weight $|v_{0x}|$ (Gedalin, Pogorelov & Roytershteyn 2023*b*). Figure 16 shows the reduced distribution function $f(x, v_x) = \int f(\boldsymbol{v}, x, z)\,\mathrm{d}v_y\,\mathrm{d}v_z\,\mathrm{d}z$.

The behaviour of ions is further illustrated by the cuts at $x = 0$. Figure 17 shows the distribution function $f(z, v_x)$ at $x = 0$. Figure 18 shows z-integrated distributions $f(v_x, v_y)$ and $f(v_x, v_z)$ for $x = 0$. Finally, figure 19 shows the magnetic field magnitude calculated using the planar stationary momentum balance (3.6). Only the values far upstream and downstream have physical sense since in the region, where rippling is still noticeable, (3.6) is not valid and should be replaced with a more complicated version (Gedalin & Ganushkina 2022). The downstream value of $|B|/B_u$ is rather close to B_d/B_u chosen in the model.

4. Discussion and conclusions

To remind a reader, the main objective of the present study was to analyse whether parameters similar to those of the observed shock crossing are consistent with a planar stationary shock profile, either non-structured or structured or non-planarity, and time dependence, e.g. in the form of ripples propagating along the shock front, are required to maintain the conservation laws. Starting with the upstream shock parameters, namely, the Alfvénic Mach number, shock angle and upstream temperature, we have shown

https://doi.org/10.1017/S0022377824001429 Published online by Cambridge University Press

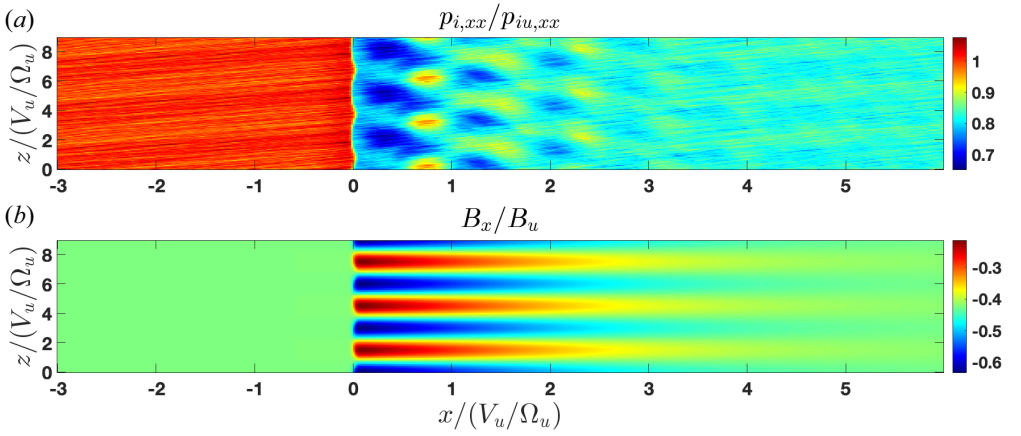

FIGURE 15. (*a*) Value of $p_{i,xx}$ as a function of x and z. (*b*) Value of B_x as a function of x and z.

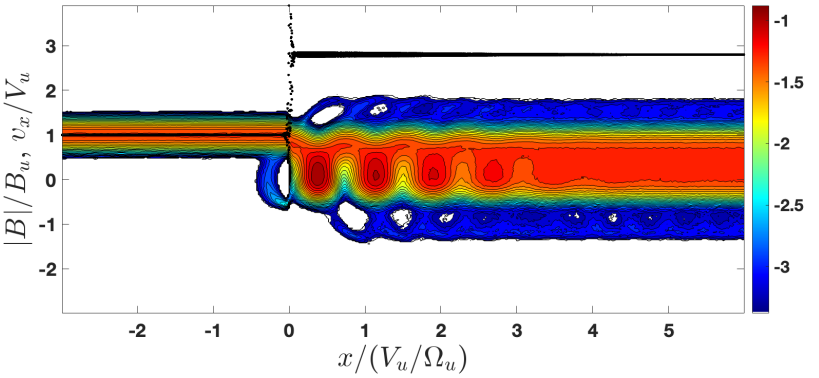

FIGURE 16. The reduced distribution function $f(x, v_x)$.

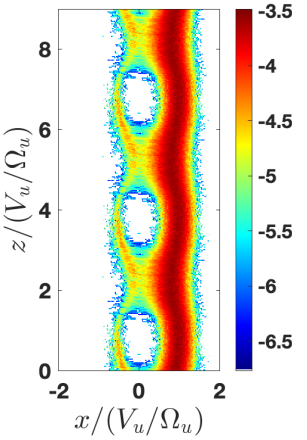

FIGURE 17. The distribution function $f(z, v_x)$ at $x = 0$.

https://doi.org/10.1017/S0022377824001429 Published online by Cambridge University Press

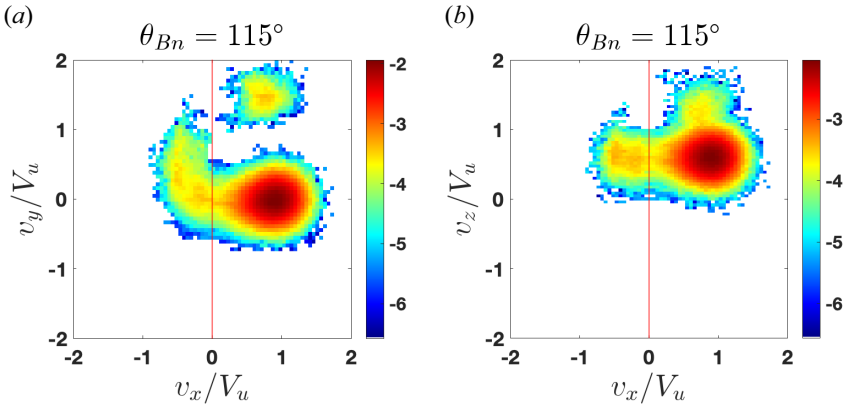

FIGURE 18. (*a*) Value of $f(v_x, v_y)$ at $x = 0$. (*b*) Value of $f(v_x, v_z)$ at $x = 0$.

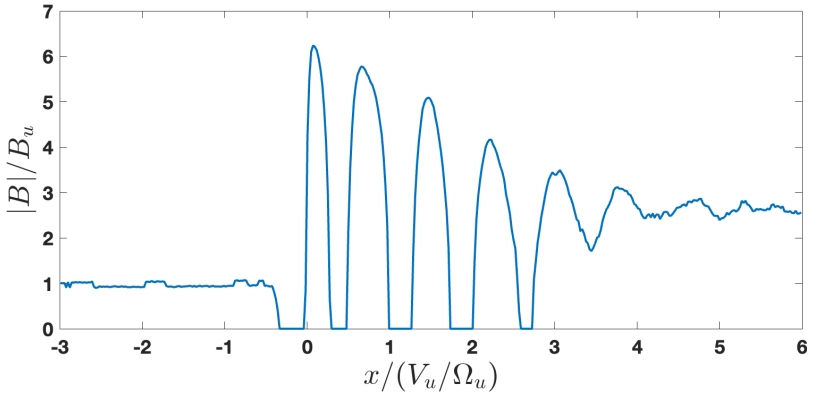

FIGURE 19. The magnetic field magnitude calculated using the planar stationary momentum balance (3.6). The derived downstream magnetic field is consistent with the chosen model magnetic field. The conversion to the downstream value starts rather quickly, less than three ion upstream convective gyroradii.

that the magnetic compression, predicted by the Rankine–Hugoniot relations, cannot be achieved in a planar stationary shock without breaking the momentum conservation (3.6) throughout the shock. Using hybrid simulations, we found that the shock with parameters similar to those of the observed shock is rippled. In the NIF, this rippling is a large-amplitude nearly monochromatic wave propagating with a constant speed along the shock front. The amplitude of the ripples is the largest in the vicinity of the ramp and overshoot, sharply dropping toward upstream and slowly decaying in the downstream region. In the frame moving with the speed of ripples along the shock front, the overall pattern of shock transition layer and the downstream region is spatially non-uniform but nearly time-independent. In NIF, where the ripples are moving, the pattern is significantly time-dependent. Observations (Johlander *et al.* 2016; Gingell *et al.* 2017; Johlander *et al.* 2018) support the numerically established picture of ripples propagating in NIF. It is not known at present whether ripples can stand in NIF. The mass, momentum and energy fluxes significantly vary in space and time but the averaged fluxes are constant throughout the shock. The 2-D simulation allowed us to determine the plausible rippling parameters which were further used for modelling the rippled shock and test particle analysis of the

https://doi.org/10.1017/S0022377824001429 Published online by Cambridge University Press

ion motion in this model. The far downstream magnetic field, derived from ion tracing in the model, is consistent with the magnetic field chosen in the model. We interpret the results of the study as an indication of a 'phase transition' from a planar stationary regime to a rippled regime, in a way similar to the transition from an almost monotonic profile in subcritical shocks to a well-structured profile in supercritical shocks. Such a 'phase transition' should occur simply because of the necessity to maintain stable fluxes of mass, momentum and energy, and would occur whatever is a specific mechanism of rippling onset. At present, we do not know what are thresholds in the parameter range required to be crossed for such a transition.

Acknowledgements

This work was partially supported by the International Space Science Institute (ISSI) in Bern, through International Team project #23-575. V.R. was partially supported by NASA grant 80NSSC21K1680 and by NSF grant 2010144. Computational resources were provided by the NASA High-End Computing (HEC) Program through the NASA Advanced Supercomputing (NAS) Division at Ames Research Center.

Editor Luís O. Silva thanks the referees for their advice in evaluating this article.

Declaration of interests

The authors report no conflict of interest.

REFERENCES

Bale, S.D., Balikhin, M.A., Horbury, T.S., Krasnoselskikh, V.V., Kucharek, H., Möbius, E., Walker, S.N., Balogh, A., Burgess, D., Lembège, B., *et al.* 2005 Quasi-perpendicular shock structure and processes. *Space Sci. Rev*. **118**, 161–203.

Balikhin, M.A., Zhang, T.L., Gedalin, M., Ganushkina, N.Y. & Pope, S.A. 2008 Venus Express observes a new type of shock with pure kinematic relaxation. *Geophys. Res. Lett*. **35**, L01103.

Burgess, D., Lucek, E.A., Scholer, M., Bale, S.D., Balikhin, M.A., Balogh, A., Horbury, T.S., Krasnoselskikh, V.V., Kucharek, H., Lembège, B., *et al.* 2005 Quasi-parallel shock structure and processes. *Space Sci. Rev*. **118**, 205–222.

Dimmock, A.P., Russell, C.T., Sagdeev, R.Z., Krasnoselskikh, V., Walker, S.N., Carr, C., Dandouras, I., Escoubet, C.P., Ganushkina, N., Gedalin, M., *et al.* 2019 Direct evidence of nonstationary collisionless shocks in space plasmas. *Sci. Adv*. **5**, eaau9926.

Farris, M.H. & Russell, C.T. 1994 Determining the standoff distance of the bow shock: Mach number dependence and use of models. *Geophys. Res. Lett*. **99**, 17.

Farris, M.H., Russell, C.T. & Thomsen, M.F. 1993 Magnetic structure of the low beta, quasi-perpendicular shock. *Geophys. Res. Lett*. **98**, 15.

Forslund, D.W. & Freidberg, J.P. 1971 Theory of laminar collisionless shocks. *Phys. Rev. Lett*. **27**, 1189–1192.

Gedalin, M. 1998 Low-frequency nonlinear stationary waves and fast shocks: hydrodynamical description. *Phys. Plasmas* **5**, 127–132.

Gedalin, M. 2015 Collisionless relaxation of non-gyrotropic downstream ion distributions: dependence on shock parameters. *J. Plasma Phys*. **81**, 905810603.

Gedalin, M. 2016 Transmitted, reflected, quasi-reflected, and multiply reflected ions in low-Mach number shocks. *Geophys. Res. Lett*. **121**, 10.

Gedalin, M. 2019*a* How non-stationary are moderately supercritical shocks? *J. Plasma Phys*. **85**, 905850505.

Gedalin, M. 2019*b* Kinematic collisionless relaxation and time dependence of supercritical shocks with alpha particles. *Astrophys. J*. **880**, 140.

Gedalin, M. 2019*c* Kinematic collisionless relaxation of ions in supercritical shocks. *Front. Phys*. **7**, 692.

GEDALIN, M. 2023 Non-locality of ion reflection at the shock front: dependence on the shock angle. *J. Plasma Phys*. **89**, 905890416.

GEDALIN, M., DIMMOCK, A.P., RUSSELL, C.T., POGORELOV, N.V. & ROYTERSHTEYN, V. 2023*a* Role of the overshoot in the shock self-organization. *J. Plasma Phys*. **89**, 905890201.

GEDALIN, M., FRIEDMAN, Y. & BALIKHIN, M. 2015 Collisionless relaxation of downstream ion distributions in low-Mach number shocks. *Phys. Plasmas* **22**, 072301.

GEDALIN, M. & GANUSHKINA, N. 2022 Implications of weak rippling of the shock ramp on the pattern of the electromagnetic field and ion distributions. *J. Plasma Phys*. **88**, 905880301.

GEDALIN, M., GOLBRAIKH, E., RUSSELL, C.T. & DIMMOCK, A.P. 2022 Theory helps observations: determination of the shock Mach number and scales from magnetic measurements. *Front. Phys*. **10**, 11.

GEDALIN, M., POGORELOV, N.V. & ROYTERSHTEYN, V. 2023*b* Scattering of ions at a rippled shock. *Astrophys. J*. **951**, 65.

GEDALIN, M. & SHARMA, P. 2023 Effect of the reflected ions on the magnetic overshoot of a collisionless shock. *Phys. Plasmas* **30**, 072905.

GINGELL, I., SCHWARTZ, S.J., BURGESS, D., JOHLANDER, A., RUSSELL, C.T., BURCH, J.L., ERGUN, R.E., FUSELIER, S., GERSHMAN, D.J., GILES, B.L., *et al.* 2017 MMS observations and hybrid simulations of surface ripples at a marginally quasi-parallel shock. *Geophys. Res. Lett*. **77**, 736–11017.

GREENSTADT, E.W., RUSSELL, C.T., FORMISANO, V., HEDGECOCK, P.C., SCARF, F.L., NEUGEBAUER, M. & HOLZER, R.E. 1977 Structure of a quasi-parallel, quasi-laminar bow shock. *J. Geophys. Res*. **82**, 651–666.

GREENSTADT, E.W., RUSSELL, C.T., GOSLING, J.T., BAME, S.J., PASCHMANN, G., PARKS, G.K., ANDERSON, K.A., SCARF, F.L., ANDERSON, R.R., GURNETT, D.A., *et al.* 1980 A macroscopic profile of the typical quasi-perpendicular bow shock - Isee 1 and 2. *Geophys. Res. Lett*. **85**, 2124–2130.

GREENSTADT, E.W., SCARF, F.L., RUSSELL, C.T., FORMISANO, V. & NEUGEBAUER, M. 1975 Structure of the quasi-perpendicular laminar bow shock. *Geophys. Res. Lett*. **80**, 502.

JOHLANDER, A., SCHWARTZ, S.J., VAIVADS, A., KHOTYAINTSEV, Y.V., GINGELL, I., PENG, I.B., MARKIDIS, S., LINDQVIST, P.A., ERGUN, R.E., MARKLUND, G.T., *et al.* 2016 Rippled quasiperpendicular shock observed by the magnetospheric multiscale spacecraft. *Phys. Rev. Lett*. **117**, 165101.

JOHLANDER, A., VAIVADS, A., KHOTYAINTSEV, Y.V., GINGELL, I., SCHWARTZ, S.J., GILES, B.L., TORBERT, R.B. & RUSSELL, C.T. 2018 Shock ripples observed by the MMS spacecraft: ion reflection and dispersive properties. *Plasma Phys. Control. Fusion* **60**, 125006.

KARIMABADI, H., VU, H., KRAUSS-VARBAN, D. & OMELCHENKO, Y. 2006 Global hybrid simulations of the earth's magnetosphere. In *Numerical Modeling of Space Plasma Flows* (ed. G.P. Zank & N.V. Pogorelov), Astronomical Society of the Pacific Conference Series, vol. 359, p. 257. Astronomical Society of the Pacific.

KENNEL, C.F. 1987 Critical Mach numbers in classical magnetohydrodynamics. *J. Geophys. Res*. **92**, 13427–13437.

KENNEL, C.F. 1988 Shock structure in classical magnetohydrodynamics. *Geophys. Res. Lett*. **93**, 8545–8557.

KENNEL, C.F., EDMISTON, J.P. & HADA, T. 1985 A quarter century of collisionless shock research. In *Collisionless Shocks in the Heliosphere: A Tutorial Review* (ed. R. G. Stone & B. T. Tsurutani) 34, pp. 1–36. American Geophysical Union.

KRASNOSELSKIKH, V., BALIKHIN, M., WALKER, S.N., SCHWARTZ, S., SUNDKVIST, D., LOBZIN, V., GEDALIN, M., BALE, S.D., MOZER, F., SOUCEK, J., *et al.* 2013 The dynamic quasiperpendicular shock: cluster discoveries. *Space Sci. Rev*. **178**, 535–598.

LEFEBVRE, B., SEKI, Y., SCHWARTZ, S.J., MAZELLE, C. & LUCEK, E.A. 2009 Reformation of an oblique shock observed by Cluster. *Geophys. Res. Lett*. **114**, A11107.

LIU, T.Z., HAO, Y., WILSON III, L.B., TURNER, D.L. & ZHANG, H. 2021 Magnetospheric multiscale observations of earth's oblique bow shock reformation by foreshock ultralow-frequency waves. *Geophys. Res. Lett*. **48**, e2020GL091184.

Livesey, W.A., Kennel, C.F. & Russell, C.T. 1982 ISEE-1 and -2 observations of magnetic field strength overshoots in quasi-perpendicular bow shocks. *Geophys. Res. Lett*. **9**, 1037–1040.

Lobzin, V.V., Krasnoselskikh, V.V., Bosqued, J.-M., Pinçon, J.-L., Schwartz, S.J. & Dunlop, M. 2007 Nonstationarity and reformation of high-Mach-number quasiperpendicular shocks: cluster observations. *Geophys. Res. Lett*. **34**, 05107.

Lobzin, V.V., Krasnoselskikh, V.V., Musatenko, K. & Dudok de Wit, T. 2008 On nonstationarity and rippling of the quasiperpendicular zone of the Earth bow shock: cluster observations. *Ann. Geophys*. **26**, 2899–2910.

Manheimer, W.M. & Spicer, D.S. 1985 Longitudinal friction and intermediate Mach number collisionless transverse magnetosonic shocks. *Phys. Fluids* **28**, 652–665.

Masters, A., Slavin, J.A., Dibraccio, G.A., Sundberg, T., Winslow, R.M., Johnson, C.L., Anderson, B.J. & Korth, H. 2013 A comparison of magnetic overshoots at the bow shocks of Mercury and Saturn. *Geophys. Res. Lett*. **118**, 4381–4390.

Mellott, M.M. & Livesey, W.A. 1987 Shock overshoots revisited. *Geophys. Res. Lett*. **92**, 13661.

Moullard, O., Burgess, D., Horbury, T.S. & Lucek, E.A. 2006 Ripples observed on the surface of the Earth's quasi-perpendicular bow shock. *Geophys. Res. Lett*. **111**, A09113.

Ofman, L., Balikhin, M., Russell, C.T. & Gedalin, M. 2009 Collisionless relaxation of ion distributions downstream of laminar quasi-perpendicular shocks. *Geophys. Res. Lett*. **114**, 09106.

Ofman, L. & Gedalin, M. 2013 Rippled quasi-perpendicular collisionless shocks: local and global normals. *Geophys. Res. Lett*. **118**, 5999–6006.

Pollock, C., Moore, T., Jacques, A., Burch, J., Gliese, U., Omoto, T., Avanov, L., Barrie, A., Coffey, V., Dorelli, J., *et al.* 2016 Fast plasma investigation for magnetospheric multiscale. *Space Sci. Rev*. **199**, 331–406.

Russell, C.T., Anderson, B.J., Baumjohann, W., Bromund, K.R., Dearborn, D., Fischer, D., Le, G., Leinweber, H.K., Leneman, D., Magnes, W., *et al.* 2016 The magnetospheric multiscale magnetometers. *Space Sci. Rev*. **199**, 189–256.

Russell, C.T., Hoppe, M.M. & Livesey, W.A. 1982*a* Overshoots in planetary bow shocks. *Nature* **296**, 45–48.

Russell, C.T., Hoppe, M.M., Livesey, W.A., Gosling, J.T. & Bame, S.J. 1982*b* ISEE-1 and -2 observations of laminar bow shocks - velocity and thickness. *Geophys. Rev. Lett*. **9**, 1171–1174.

Sagdeev, R.Z. 1966 Cooperative phenomena and shock waves in collisionless plasmas. *Rev. Plas. Phys*. **4**, 23.

Scudder, J.D., Aggson, T., Aggson, T.L., Mangeney, A., Lacombe, C. & Harvey, C.C. 1986 The resolved layer of a collisionless, high beta, supercritical, quasi-perpendicular shock wave. I - Rankine-Hugoniot geometry, currents, and stationarity. *Geophys. Res. Lett*. **91**, 11019–11052.

Sharma, P. & Gedalin, M. 2023 Non-specular ion reflection at quasiperpendicular collisionless shock front. *J. Plasma Phys*. **89**, 905890505.

Sundberg, T., Boardsen, S.A., Slavin, J.A., Uritsky, V.M., Anderson, B.J., Korth, H., Gershman, D.J., Raines, J.M., Zurbuchen, T.H. & Solomon, S.C. 2013 Cyclic reformation of a quasi-parallel bow shock at Mercury: MESSENGER observations. *Geophys. Res. Lett*. **118**, 6457–6464.

Tatrallyay, M., Gevai, G., Apathy, I., Schwingenschuh, K., Zhang, T.L., Kotova, G.A., Verigin, M.I., Livi, S. & Rosenbauer, H. 1997 Magnetic field overshoots in the Martian bow shock. *J. Geophys. Res*. **102**, 2157–2164.

Tatrallyay, M., Luhmann, J.G. & Research, C.R.A.I.S. 1984 Magnetic field overshoots in the Venus bow shock. *Adv. Space Res*. **4**, 283–286.

Tiu, D., Cairns, I.H., Yuan, X. & Robinson, P.A. 2011 Evidence for reformation of the Uranian bow shock: hybrid simulations and comparisons with Voyager data. *Geophys. Res. Lett*. **116**, A04228.

Torbert, R.B., Russell, C.T., Magnes, W., Ergun, R.E., Lindqvist, P.A., Le Contel, O., Vaith, H., Macri, J., Myers, S., Rau, D., *et al.* 2016 The FIELDS instrument suite on MMS: scientific objectives, measurements, and data products. *Space Sci. Rev*. **199**, 105–135.

Winske, D., Karimabadi, H., Le, A.Y., Omidi, N.N., Roytershteyn, V. & Stanier, A.J. 2023 *Hybrid-Kinetic Approach: Massless Electrons*, 63–91. Springer International Publishing.

Zhou, X. & Smith, E.J. 2015 Supercriticality of ICME and CIR shocks. *Geophys. Res. Lett*. **120**, 1526–1536.